LETTER

https://doi.org/10.1038/s41586-018-0031-4

# Low-loss plasmon-assisted electro-optic modulator

Christian Haffner[1]*, Daniel Chelladurai[1], Yuriy Fedoryshyn[1], Arne Josten[1], Benedikt Baeuerle[1], Wolfgang Heni[1], Tatsuhiko Watanabe[1], Tong Cui[1], Bojun Cheng[1], Soham Saha[3], Delwin L. Elder[2], Larry. R. Dalton[2], Alexandra Boltasseva[3], Vladimir M. Shalaev[3], Nathaniel Kinsey[4] & Juerg Leuthold[1]*

**For nearly two decades, researchers in the field of plasmonics[1]—which studies the coupling of electromagnetic waves to the motion of free electrons near the surface of a metal[2]—have sought to realize subwavelength optical devices for information technology[3–6], sensing[7,8], nonlinear optics[9,10], optical nanotweezers[11] and biomedical applications[12]. However, the electron motion generates heat through ohmic losses. Although this heat is desirable for some applications such as photo-thermal therapy, it is a disadvantage in plasmonic devices for sensing and information technology[13] and has led to a widespread view that plasmonics is too lossy to be practical. Here we demonstrate that the ohmic losses can be bypassed by using 'resonant switching'. In the proposed approach, light is coupled to the lossy surface plasmon polaritons only in the device's off state (in resonance) in which attenuation is desired, to ensure large extinction ratios between the on and off states and allow subpicosecond switching. In the on state (out of resonance), destructive interference prevents the light from coupling to the lossy plasmonic section of a device. To validate the approach, we fabricated a plasmonic electro-optic ring modulator. The experiments confirm that low on-chip optical losses, operation at over 100 gigahertz, good energy efficiency, low thermal drift and a compact footprint can be combined in a single device. Our result illustrates that plasmonics has the potential to enable fast, compact on-chip sensing and communications technologies.**

Telecommunication devices such as electro-optic modulators must feature low insertion loss (the reduction of signal power resulting from insertion of the device into the transmission line) while providing a large change in phase ($\Delta n$) or amplitude ($\Delta\alpha$) accumulated over a short device length[14]. Beyond that, modulators should offer low driving voltages and high-speed operation.

In recent years, silicon photonics has emerged that has low propagation losses (of the order of dB cm$^{-1}$) but has struggled to achieve large modulation depth (that is, $\Delta n$ and $\Delta\alpha$) for submillimetre devices[15]. State-of-the-art devices maximize their modulation through the use of resonant structures[16], enabling compact (few square micrometres) and energy-efficient components[17,18]. And although large quality factors ($Q$-factors, large values indicate low energy losses), of the order of several thousand, allow considerable reduction of the driving voltage, they limit the speed and increase the sensitivity of devices to temperature and fabrication fluctuations[19]. More recently, surface plasmonic polariton (SPP) devices have exploited the extreme confinement of light to achieve exceptional modulation of phase and amplitude within a few micrometres[3,20]. However, the metals that give plasmonics such promise are also the largest hindrance, as such devices suffer from large on-state loss (of the order of dB μm$^{-1}$). To combat plasmonic losses, some devices use hybrid plasmonic–photonic modes[4,6,21] whereas others minimize the length of the active section[5,22]. Still, typical insertion losses of 10 dB due to plasmonic propagation and photonic-to-plasmonic mode conversion remain a concern for high-speed state-of-the-art devices[5,6]. Thus, plasmonic on-chip technologies have been unable to replace the existing photonic or electronic solutions.

We propose an approach in which losses in plasmonic waveguides can be selectively used or bypassed to achieve low insertion loss, strong modulation, compact footprint and high speed, simultaneously. Previously, the goal has been to reduce the ohmic loss as much as possible to minimize the device's loss in the on state. Instead, we show that plasmonic losses can be tolerated by designing the device geometry such that light passes through the lossy section when required (in the off state). To achieve this, we use a plasmonic ring resonator coupled to a buried low-loss silicon photonic waveguide (see Fig. 1).

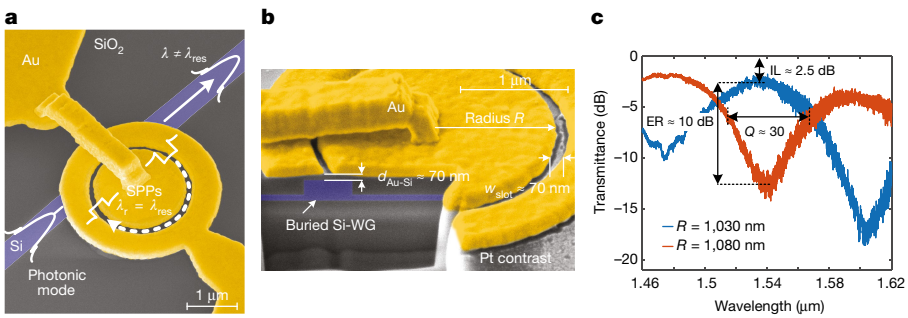


**Fig. 1 | False-coloured scanning electron microscopy (SEM) image of a plasmonic ring resonator and the corresponding transmittance. a**, Top view; **b**, cross-section of the resonator. Photonic modes propagating in the buried silicon waveguide (Si-WG) resonator couple partially to the SPPs in the MIM ring when the resonance condition is fulfilled. While out of resonance, operation results in low-loss light transmission. $d_{Au-Si}$, vertical distance between the gold ring resonator and the buried silicon. **c**, Passive measurements of two identical ring resonators that differ only in radii (blue, 1,030 nm; red, 1,080 nm). To estimate the optical properties of such plasmonic ring resonators through passive measurement, we compare the two resonators to determine the insertion losses (IL), extinction ratio (ER) and $Q$-factor at 1.54 μm. Here we use the off-resonance resonator (blue) to measure the insertion loss, and the on-resonance resonator (red) to extract the $Q$-factor at 1.54 μm. The difference between the red and blue reveals the extinction ratio. With the resonant approach, insertion losses of about 2.5 dB are measured with extinction ratios above 10 dB.

[1]ETH Zurich, Institute of Electromagnetic Fields (IEF), Zurich, Switzerland. [2]Department of Chemistry, University of Washington, Seattle, WA, USA. [3]School of Electrical & Computer Engineering and Birck Nanotechnology Center, Purdue University, West Lafayette, IN, USA. [4]Department of Electrical and Computer Engineering, Virginia Commonwealth University, Richmond, VA, USA.
*e-mail: haffnerc@ethz.ch; leuthold@ethz.ch

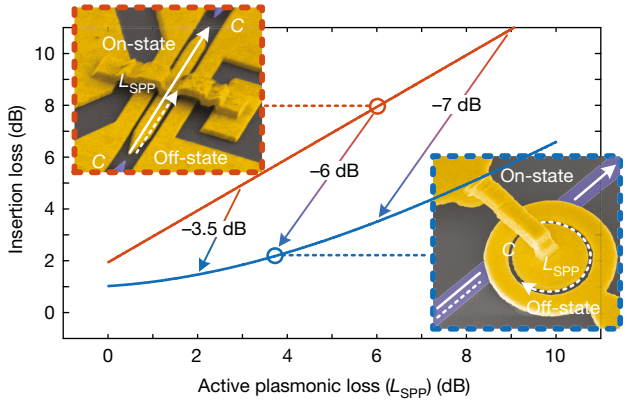


**Fig. 2 | Theoretical loss advantage of critical coupled resonant device over non-resonant push–pull MZ device.** The insertion losses are plotted against the active plasmonic loss ($L_{SPP}$) in the slot waveguide of the MZ modulator (left inset, red) and resonator (right inset, blue). Losses can be reduced by more than 6 dB. This is for the following reasons: (i) the bypassing mechanism: only a fraction of light experiences plasmonic losses; (ii) resonant enhancement: the resonators achieve the same modulation depth ($\Delta T$) for shorter active plasmonic sections than their non-resonant counterparts (indicated by the horizontal shift of the arrows); and (iii) coupling scheme: non-resonant approaches require two photonic/SPP converters whereas resonant approaches require only one.

Unlike previous approaches, which aim to reduce the resonator loss to realize high-$Q$ cavities or lasing[7,23–26], our resonator exhibits typical propagation losses within the plasmonic cavity and mostly bypasses this lossy section in the on state through destructive interference. Using this design, we demonstrate a plasmonic modulator that can meet the key performance metrics of modern optical communications links.

Figure 1 shows the proposed device geometry, which comprises a gold metal–insulator–metal (MIM) slot waveguide ring coupled to a buried silicon bus waveguide, forming a notch filter with a resonant wavelength of $\lambda_{res}$ (see section II of the Supplementary Information). The slot waveguide is filled with an organic electro-optic (OEO) material which alters the device's resonance condition through the Pockels effect ($\Delta n_{SPP}$)[27]. This permits fast and selective use of the resonator's ohmic loss to attenuate the signal ($\Delta\alpha$) in the bus waveguide by applying a voltage.

Figure 1c shows the measured transmittance over the wavelength of two representative devices that differ slightly in radius. The difference in radius does not affect their optical properties (insertion loss, extinction ratio, $Q$-factor), but results in a distinct off-resonance ($\lambda_0 \neq \lambda_{res}$) and on-resonance ($\lambda_0 = \lambda_{res}$) behaviour at the telecommunication wavelength of 1.54 μm. The off-resonance ring reveals an insertion loss of about 2.5 dB, the on-resonance ring shows a $Q$-factor of about 30, and their difference in transmittance indicates an extinction ratio of about 10 dB. We note that non-resonant devices based on similar-length MIM waveguides feature an insertion loss ranging from 8 dB to 10 dB (refs. [5,6,22]).

The reduced insertion loss can be understood by comparing the exemplary operating principles of a non-resonant Mach–Zehnder modulator (MZ)[5] (Fig. 2, left inset; white solid arrow indicates the plasmonic section) and a resonant ring (Fig. 2, right inset). The insertion loss of the device is a function of its coupling efficiency, geometry and accumulated ohmic loss. In both concepts, light couples to and from the plasmonic structure with a coupling efficiency $C$. A transmission modulation is then induced by the Pockels effect over an active plasmonic section of length or circumference $l$. The modulation depth $\Delta T$, where $T$ is transmittance, and also the loss $L_{SPP}$ scale with the length of the active plasmonic section[6]. Figure 2 shows the overall insertion loss over the $L_{SPP}$ in the active plasmonic area for a MZ (red curve) and for a critically coupled resonator (blue curve). The arrows in the plot indicate the performance of devices with an equal $\Delta T$.

The following points arise from Fig. 2. First, the resonator's total loss is always smaller than that of a MZ modulator (blue curve < red curve), owing to the bypassing mechanism[28]. The insertion loss increases with $L_{SPP}$ (that is, inverse to the cavity's $Q$-factor) as the critical coupling condition requires that more light couples to the plasmonic section. Second, the resonator has an insertion loss 1 dB lower than that of the MZ at $L_{SPP} \approx 0$ dB. This is because the non-resonant device requires two photonic–SPP converters as both the on state and the off state propagate through the plasmonic section. Ohmic losses in the converters limit the conversion efficiency to about 1 dB (refs. [22,29]). In contrast, the selection mechanism of the resonator (on state: bus waveguide; off state: ring) requires a converter which couples only a fraction of the light to the ring. Third, in the ring we take advantage of the resonantly enhanced $\Delta T$ to reduce the device length (see section VII of the Supplementary Information). For our resonant structures, we have calculated an enhancement of about 1.5. Consequently, our ring with a circumference of $l = 6$ μm ($L_{SPP} \approx 4$ dB) offers the same transmittance change as a MZ of $l = 9$ μm ($L_{SPP} \approx 6$ dB). In total, the ring device offers an advantage of 6 dB insertion loss over the MZ modulator. Losses can be further reduced by under-coupling the resonator, as limited extinction ratios of 10 dB are sufficient for many practical applications[30].

To illustrate the modulation performance ($\Delta T$) of the plasmonic resonator, the effective refractive index for SPPs ($\Delta n_{SPP}$) is altered by applying a bias between the inner and outer rings[27]. Figure 3a shows the transmitted power versus applied voltage for a probe wavelength of approximately 1.52 μm. We observed an insertion loss < 3 dB, an extinction ratio of about 10 dB and a linear response (dashed green line) for a peak voltage of 3.5 V with an extinction ratio of about 6 dB. This performance in terms of insertion loss and extinction ratio is similar to that of well-developed complementary metal oxide semiconductor (CMOS) photonic resonators[19]. We estimate that operation under a digital peak-to-peak driving voltage (1 V)[19] will soon be achievable by using other plasmonic materials such as silver or copper, using the newest OEO materials and improving fabrication (see Methods: Future

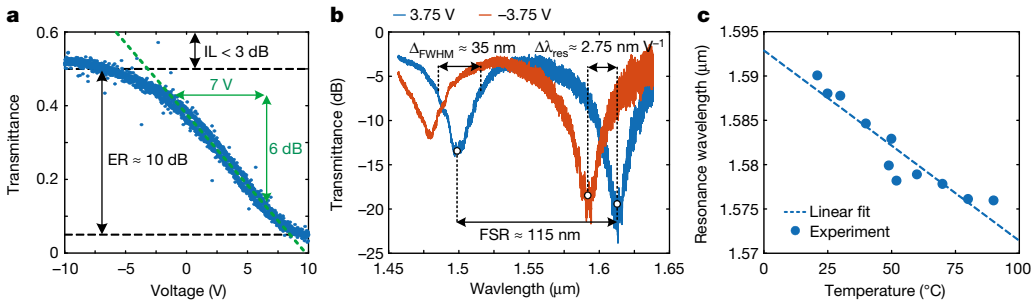


**Fig. 3 | Sensitivity and stability of the plasmonic resonator. a**, Voltage sensitivity of the resonator's transmittance. IL, insertion loss; ER, extinction ratio. Probe wavelength 1.52 μm. **b**, Sensitivity of the ring as a function of the wavelength. A change ($\Delta n_{slot} \approx 0.03$) in the refractive index of the slot-filling material causes a large change in the resonance wavelength (blue/red). FSR, free spectral range. **c**, The resonator shows stable operation across a large thermal variation. The dashed line indicates a slope of $\Delta\lambda_{res}/(\Delta_{FWHM}\Delta T) \approx 0.4\%\ K^{-1}$. These characteristics make the plasmonic MIM-ring resonator a promising candidate in the field of optical modulators and sensors.

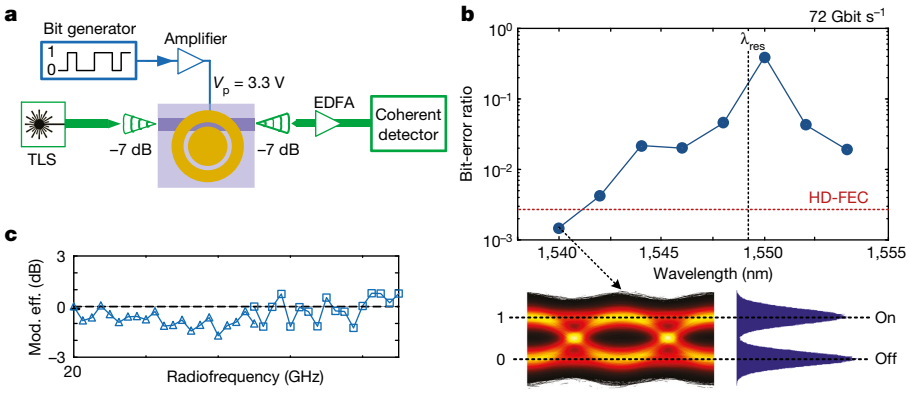


**Fig. 4 | High-speed data experiments with a plasmonic ring resonator used as an electro-optic modulator. a**, The experimental set-up. EDFA, erbium-doped fibre amplifier; TLS, tuneable laser source; $V_p$, peak voltage. **b**, BER versus wavelength for a resonator with $\lambda_{res} = 1{,}549$ nm. BERs below the HD-FEC limit show successful data modulation and detection without the use of a temperature control. The BER increases at the resonance wavelength as expected from the notch-filter response of the resonator. **c**, The bandwidth of the plasmonic resonator, which is beyond 110 GHz. Mod. eff., modulation efficiency.

improvements). To highlight the mechanism of the modulation, the transmission of the device was measured under a positive and negative bias ($\pm 3.75$ V) as a function of wavelength (see Fig. 3b). This results in a normalized sensitivity, $S_\lambda/\Delta_{FWHM} = \Delta\lambda_{res}/(\Delta_{FWHM}\Delta n)$, where $\Delta_{FWHM}$ is the full-width at half-maximum, of about 17 RIU$^{-1}$ (RIU is refractive index unit), assuming a relative change in the OEO refractive index of about 0.03. This can be compared to commercial SPR sensors that achieve values of 50 RIU$^{-1}$ by using a free-space Kretschmann configuration[31]. Therefore, our approach is already close to the non-integrated free-space approaches.

The moderate $Q$-factor guarantees a high operational speed and provides good thermal stability. For example, the measured resonance frequency is plotted in Fig. 3c over a temperature range from 20 °C up to 90 °C. In this case, the resonant frequency is found to follow a linear trend line with a slope of about 0.4% K$^{-1}$. The insensitivity of the low-$Q$ plasmonic resonator to temperature fluctuations is in strong contrast to high-$Q$ photonic resonators, which are two orders of magnitude more sensitive to temperature fluctuations (approximately 100% K$^{-1}$)[18]. This is extremely beneficial for applications in which strong temperature fluctuations occur. For example, a low-$Q$ plasmonic resonant sensor or modulator would be immune to thermal fluctuations of $\pm 5$ °C which normally occur in CPUs, whereas high-$Q$ photonic resonators require power-consuming temperature controls to maintain operation[19]. Furthermore, the moderate $Q$ factors are beneficial for high-speed operation, as desired in electro-optic modulators. As a result, we are able to push the bandwidth of a resonant electro-optic modulator well beyond 100 GHz (see Methods section 'Speed limitations'). In comparison, photonic resonators are more likely to be limited to bandwidths of about 20 GHz and below[18,19].

Subsequently, we performed high-speed data experiments to demonstrate the robustness, high speed and low power switching capability. Although the 'resonant switching' principle can also be used to optimize sensors, we focus on high-speed applications because their sensitivity and stability requirements are stricter.

In the experiment of Fig. 4a, the peak driving voltage was approximately 3.3 V, and the laser wavelength was varied to capture the response of the modulator. Low device losses of 2.5 dB and fibre-to-silicon waveguide losses of about 7 dB resulted in fibre-to-fibre coupling losses of 16.5 dB, enabling successful operation with low laser powers of 4 dBm and below. The resulting bit-error ratio (BER) versus wavelength for a 72 Gbit s$^{-1}$ signal is shown in Fig. 4b, where a peak in the BER is observed at $\lambda_{res}$ (dashed line). The BER shows a peak because the change of transmittance ($\Delta T$) has a symmetric response to voltage when the probing wavelength $\lambda$ equals $\lambda_{res}$. Consequently, we confirmed that the operating mechanism relies on amplitude modulation. Off-resonance, the BER quickly dropped to about $1 \times 10^{-3}$, which is below the hard-decision forward error correction (HD-FEC) limit and allows for successful data modulation and detection[32]. No thermal heater was required for stabilization. Additionally, we reduced the data rate to 36 Gbit s$^{-1}$ and 18 Gbit s$^{-1}$ and found BERs of about $2 \times 10^{-6}$ and $< 1 \times 10^{-6}$, respectively, indicating that the BER at 72 Gbit s$^{-1}$ is mainly limited by the electrical equipment (see Methods: Data experiments). We estimate the energy consumption of the modulator to be about 12 fJ bit$^{-1}$ at 72 Gbit s$^{-1}$ (ref. [14]) for a device capacitance of 1.1 fF.

We have demonstrated that low-$Q$ resonant designs using highly confined SPPs can enable low-loss active plasmonic devices with a good modulation depth. We believe that our approach—unlike conventional resonant photonics—breaks the trade-off between sensitivity (high-$Q$) on the one hand and speed and temperature stability (low-$Q$) on the other. Our work can be seen as a step towards practical plasmonics that ultimately serves as a compact and fast gateway between electronics (local signal processing) and photonics (broad bandwidth and low-loss data stream). The proposed slot waveguide approach could be of interest for sensing, because the resonant response could be exploited for many other material systems ranging from low-index materials such as aqueous solutions to high-index materials such as silicon.

## Online content

Any Methods, including any statements of data availability and Nature Research reporting summaries, along with any additional references and Source Data files, are available in the online version of the paper at https://doi.org/10.1038/s41586-018-0031-4.

Received: 30 October 2017; Accepted: 28 January 2018;
Published online 25 April 2018.

1. Maier, S. A. et al. Plasmonics—a route to nanoscale optical devices. *Adv. Mater.* **13**, 1501–1505 (2001).
2. Gramotnev, D. K. & Bozhevolnyi, S. I. Plasmonics beyond the diffraction limit. *Nat. Photonics* **4**, 83–91 (2010).
3. Dionne, J. A., Diest, K., Sweatlock, L. A. & Atwater, H. A. PlasMOStor: a metal–oxide–Si field effect plasmonic modulator. *Nano Lett.* **9**, 897–902 (2009).
4. Sorger, V. J., Lanzillotti-Kimura Norberto, D., Ma, R.-M. & Zhang, X. Ultra-compact silicon nanophotonic modulator with broadband response. *Nanophotonics* **1**, 17–22 (2012).
5. Haffner, C. et al. All-plasmonic Mach–Zehnder modulator enabling optical high-speed communication at the microscale. *Nat. Photon.* **9**, 525–528 (2015).
6. Keeler, G. A. et al. in *Optical Fiber Communication Conference* Th3I.1 (Optical Society of America, 2017).
7. Min, B. et al. High-Q surface-plasmon-polariton whispering-gallery microcavity. *Nature* **457**, 455–458 (2009).
8. Brolo, A. G. Plasmonics for future biosensors. *Nat. Photonics* **6**, 709–713 (2012).
9. Cai, W., Vasudev, A. P. & Brongersma, M. L. Electrically controlled nonlinear generation of light with plasmonics. *Science* **333**, 1720–1723 (2011).
10. Kauranen, M. & Zayats, A. V. Nonlinear plasmonics. *Nat. Photonics* **6**, 737–748 (2012).

11. Ndukaife, J. C. et al. Long-range and rapid transport of individual nano-objects by a hybrid electrothermoplasmonic nanotweezer. *Nat. Nanotech.* **11**, 53–59 (2016).
12. Hirsch, L. R. et al. Nanoshell-mediated near-infrared thermal therapy of tumors under magnetic resonance guidance. *Proc. Natl Acad. Sci. USA* **100**, 13549–13554 (2003).
13. Khurgin, J. B. How to deal with the loss in plasmonics and metamaterials. *Nat. Nanotech.* **10**, 2–6 (2015).
14. Miller, D. A. B. Attojoule optoelectronics for low-energy information processing and communications; a tutorial review. *J. Lightwave Technol.* https://doi.org/10.1109/JLT.2017.2647779 (2017).
15. Reed, G. T., Mashanovich, G., Gardes, F. Y. & Thomson, D. J. Silicon optical modulators. *Nat. Photon.* **4**, 518–526 (2010); erratum *Nat. Photon.* **4**, 660 (2010).
16. Vahala, K. J. Optical microcavities. *Nature* **424**, 839–846 (2003).
17. Xu, Q., Schmidt, B., Pradhan, S. & Lipson, M. Micrometre-scale silicon electro-optic modulator. *Nature* **435**, 325–327 (2005).
18. Timurdogan, E. et al. An ultralow power athermal silicon modulator. *Nat. Commun.* **5**, 4008 (2014).
19. Sun, C. et al. Single-chip microprocessor that communicates directly using light. *Nature* **528**, 534–538 (2015).
20. Emboras, A. et al. Atomic scale plasmonic switch. *Nano Lett.* https://doi.org/10.1021/acs.nanolett.5b04537 (2015).
21. Oulton, R. F., Sorger, V. J., Genov, D. A., Pile, D. F. P. & Zhang, X. A hybrid plasmonic waveguide for subwavelength confinement and long-range propagation. *Nat. Photon.* **2**, 496–500 (2008).
22. Zhu, S., Lo, G. Q. & Kwong, D. L. Phase modulation in horizontal metal–insulator–silicon–insulator–metal plasmonic waveguides. *Opt. Express* **21**, 8320–8330 (2013).
23. Hill, M. T. et al. Lasing in metallic-coated nanocavities. *Nat. Photon.* **1**, 589–594 (2007).
24. Bozhevolnyi, S. I., Volkov, V. S., Devaux, E., Laluet, J.-Y. & Ebbesen, T. W. Channel plasmon subwavelength waveguide components including interferometers and ring resonators. *Nature* **440**, 508–511 (2006).
25. Kress, S. J. P. et al. A customizable class of colloidal-quantum-dot spasers and plasmonic amplifiers. *Sci. Adv.* **3**, e1700688 (2017).
26. Zhu, W. et al. Surface plasmon polariton laser based on a metallic trench Fabry–Perot resonator. *Sci. Adv.* **3**, e1700909 (2017).
27. Sun, S. S. & Dalton, L. R. *Introduction to Organic Electronic and Optoelectronic Materials and Devices* 28–37 (Taylor & Francis, Boca Raton, 2008).
28. Zanotto, S., Morichetti, F. & Melloni, A. Fundamental limits on the losses of phase and amplitude optical actuators. *Laser Photonics Rev.* **9**, 666–673 (2015).
29. Delacour, C. et al. Efficient directional coupling between silicon and copper plasmonic nanoslot waveguides: toward metal–oxide–silicon nanophotonics. *Nano Lett.* **10**, 2922–2926 (2010).
30. Bogaerts, W. et al. Silicon microring resonators. *Laser Photonics Rev.* **6**, 47–73 (2012).
31. Becker, J., Trügler, A., Jakab, A., Hohenester, U. & Sönnichsen, C. The optimal aspect ratio of gold nanorods for plasmonic bio-sensing. *Plasmonics* **5**, 161–167 (2010).
32. Chang, F., Onohara, K. & Mizuochi, T. Forward error correction for 100 G transport networks. *IEEE Commun. Mag.* **48**, https://doi.org/10.1109/MCOM.2010.5434378 (2010).


**Acknowledgements** We thank U. Drechsler and H.-R. Benedickter for their technical assistance. We acknowledge partial funding of this project by the EU Project PLASMOFAB (688166), by ERC grant PLASILOR (640478), by the National Science Foundation (NSF) (DMR-1303080) and by the Air Force Office of Scientific Research grants (FA9550-15-1-0319 and FA9550-17-1-0243). N.K. acknowledges support from the Virginia Microelectronics Consortium and the Virginia Commonwealth University Presidential Research Quest Fund. This work was carried out at the BRNC Zurich and ETH Zurich.

**Reviewer information** *Nature* thanks J. Khurgin and the other anonymous reviewer(s) for their contribution to the peer review of this work.

**Author contributions** C.H., N.K., V.M.S., A.B. and J.L. conceived the concept and supervised the project. C.H., D.C., S.S. and T.C. designed the modulator and developed the analytical framework for fast optimization. T.W. designed the photonic grating coupler. C.H., D.C. and Y.F. fabricated the modulator and developed the required process technology. B.C. developed a focused ion beam process to image the cross-section with minimal destructive influence on the suspended bridge. D.L.E., W.H., C.H. and L.R.D. developed, synthesized and implemented the poling procedure of the OEO material for plasmonic ring resonators. C.H. and J.L. designed the experiments. C.H., D.C. and T.C. performed the passive characterization. C.H. performed the temperature sensitivity, d.c. switching and electro-optic bandwidth experiments. B.B., A.J. and C.H. performed the high-speed data experiment. B.B. and A.J. designed, calibrated and automated the high-speed data experiment. B.B. and A.J. developed the digital-signal processing for data generation and analysis of the high-speed data experiment. All authors discussed and analysed the data. C.H., N.K., D.C. and J.L. wrote the manuscript.

**Competing interests** The authors declare no competing financial interests.

**Additional information**
**Extended data** is available for this paper at https://doi.org/10.1038/s41586-018-0031-4.
**Supplementary information** is available for this paper at https://doi.org/10.1038/s41586-018-0031-4.
**Reprints and permissions information** is available at http://www.nature.com/reprints.
**Correspondence and requests for materials** should be addressed to C.H. or J.L.
**Publisher's note:** Springer Nature remains neutral with regard to jurisdictional claims in published maps and institutional affiliations.

## METHODS

**Future improvements.** The plasmonic material strongly influences the performance of the ring resonator in terms of losses and resonant enhancement. In this section, we discuss the influence of various plasmonic materials and we show that the modulator performance improves when replacing gold with copper (CMOS-compatible) or silver (lowest loss).

In a first step, we investigate the unloaded $Q$-factor for different plasmonic metals. Extended Data Fig. 1 shows the unloaded quality factor $Q$ as a function of the slot width and the radius for Au (panel a), Cu (b) and Ag (c).

Both Cu and Ag feature higher $Q$-factors than Au. When changing the plasmonic metal from Au to Ag, the $Q$-factor is more than doubled for geometries dominated by propagation loss (140 for Ag versus 60 for Au). Each material shows the trade-off between propagation loss and bending loss resulting in the characteristic triangular contour lines (see section III of the Supplementary Information). Furthermore, using low-loss materials such as Ag will increase not only the intrinsic $Q$-factor but also the coupling efficiency $C$. Three-dimensional simulations indicate that $C$ increases from 0.8 to 0.9.

Besides the plasmonic material, the OEO material provides an additional path for further improvement. Recent experiments have shown that electro-optic coefficients over 300 pm $V^{-1}$ are achievable by operating in close vicinity of the OEO material resonance ($\lambda \approx 1{,}250$ nm)[33]. Additionally, other OEO materials such as JRD1 show electro-optic coefficients over 300 pm $V^{-1}$ (refs. [34–36]).

To evaluate the influence of these improvements on the modulator performance, Extended Data Fig. 1 shows the wavelength-dependent transmittance of a MIM-ring resonator obtained by the analytic model (equation (2) in the Supplementary Information). Extended Data Fig. 1d shows the transmittance for Au while Extended Data Fig. 1e includes the possible improvements with Ag and JRD1 (electro-optic coefficient of 300 pm $V^{-1}$). The radius is 1 μm, the slot width is 80 nm and the outer electrode height is 350 nm. The solid lines correspond to positive (blue) and negative (red) biasing of 2 V.

Such improved configurations offer through-port insertion loss as small as 0.5 dB (Ag) compared with 1.5 dB (Au). Furthermore, the switching sensitivity is increased because of the higher nonlinearity (sensitivity increase by 3 ×) and the larger $Q$-factor (2 ×). Thus, the absolute insertion loss reduces from 4.3 dB to 1.2 dB, and the extinction ratio increases from 2 dB to 18 dB when driven with ± 2 V at the chosen probing wavelength (vertical green line, Extended Data Fig. 1d, e). Thus, low-power CMOS transistors may drive the plasmonic resonators without the help of electrical amplification. This would reduce the total energy consumption of the modulators to below 1 fJ per bit.

**Alternative active materials for modulation and sensing.** Here, we discuss the influence of the refractive index of the slot material on the unloaded $Q$-factor of plasmonic ring resonators. The active material could be either an OEO material for modulation or a biosensitive material for sensing purposes. Extended Data Fig. 2 shows the simulated $Q$-factors for different slot widths and radii. The simulated refractive indices range from 1.33 up to 3.48 as shown in subplots in Extended Data Fig. 2a to h.

All material systems achieve $Q$-factors above 30. The refractive index of the active material strongly influences the bending and propagation losses. In the case of low $n_{slot}$, for Extended Data Fig. 2a and b, the $Q$-factor is mainly limited by bending losses for all slot widths as indicated by the diagonal contour lines (dashed lines). This behaviour changes when $n_{slot}$ increases to 1.75 (Extended Data Figs. 2c) or 2 (Extended Data Fig. 2d) and typical triangular contour lines can be observed highlighting the trade-off between bending losses and propagation losses (see section IV of the Supplementary Information). A further increase of the refractive index results in dominating propagation losses. The triangular shape of the contour line changes to contour lines parallel to the bottom axis (radius). In this region (see subplots in Extended Data Fig. 2e to h), the $Q$-factor drops for the same geometrical parameters as propagation loss increases with the refractive index[37].

The subplots shown in Extended Data Fig. 2a, c, e and h are of most interest as they represent materials that can be used for sensing: (a) $n_{slot} = 1.33$ ($H_2O$); or for electro-optic modulation: (c) $n_{slot} = 1.75$ (OEO)[35]; (e) $n_{slot} = 2.25$ (barium titanate, BTO)[38]; and (h) $n_{slot} = 3.48$ (Si)[22].

**Sample fabrication.** All reported devices were processed on silicon-on-insulator wafers with a 220-nm-thick Si device layer and 3-μm-thick buried oxide. Electron beam lithography (Vistec EBPG5200) in combination with ICP-RIE (Oxford Plasmalab System 100) were applied to pattern the Si photonic components. A positive tone resist (poly(methyl methacrylate), PMMA) and a negative tone resist (hydrogen silsesquioxane, HSQ) were used as masks to define the partially (70 nm) and fully (220 nm) etched Si structures, respectively[39]. Planarization of the patterned Si structures was realized by spin-coating the samples with a 1-μm-thick HSQ layer followed by rapid thermal annealing to convert HSQ to $SiO_2$ (ref. [40]). We observed thickness variations of ± 10 nm with a periodicity of 50 μm throughout the chip. This does not affect device performance, as the footprint of the resonators is much smaller than the periodicity. We controlled the coupling between the ring and bus waveguide by using the following protocol, which enabled us to adjust the average vertical spacing between the gold ring and silicon bus ($d_{Au-Si}$) to within 5 nm of the target value. First, we use an electron-beam-patterned PMMA resist mask to open silicon etch marks placed next to the device to measure the HSQ thickness during the following wet etching process. Afterwards, we used a second e-beam patterned PMMA resist to locally etch down the $SiO_2$ over the bus waveguide to the desired spacing $d_{Au,Si} = 70 \pm 10$ nm by using a buffered HF (7:1) solution. The slow etch-rate of 1.2 nm $s^{-1}$ enables good process control. Note that the spin-coating process rather than the wet etching process introduces the uncertainty of ± 10 nm. Contact pads, outer rings (height $h = 350$ nm), inner rings ($h = 150$ nm) and bridges ($h = 350$ nm) were produced with a sequence of e-beam lithography, e-beam evaporation of Au and lift-off processes as reported in ref. [5]. Extended Data Fig. 3 shows a tilted top view of the fabricated ring resonator before the bridge fabrication step. The height of the outer electrode is 350 nm, whereas the inner electrode is only 150 nm, enabling a reduction of the bending losses (see section IV of the Supplementary Information).

We characterized the geometry of all devices using SEM for better comparison to simulations. This allows us to estimate parameters such as the electro-optic coefficient, $r_{33}$. Finally, the binary OEO material (75%HD-BB-OH/25%YLD124)[41] was spin-coated then poled at its glass transition temperature (115 °C) by applying electric fields of approximately 130 V $\mu m^{-1}$. It has been shown[33] that this OEO material allows operation up to 80 °C.

We chose the following design parameter sets: slot widths of 80 nm and 100 nm with radii ranging from 900 nm to 1,200 m and 1,400 nm to 1600 nm.

**Passive characterization.** We determined the transmittance of the resonators by subtracting back-to-back measurements of structures that comprise the same grating couplers and photonic waveguides but lack the plasmonic section. The standard deviation of the back-to-back measurements was below ± 0.5 dB over the whole wavelength range of the tunable laser (1,465 nm to 1,635 nm). We measured the passive spectrum for various input power up to 10 dBm and did not observe any drift of the resonance wavelength due to self-heating. To prevent any self-heating, we set the laser power to 0 dBm for the passive characterization.

Extended Data Fig. 4 shows two histograms of the measured insertion loss (Extended Data Fig. 4a) and extinction ratio (Extended Data Fig. 4b) of 23 ring resonators with targeted slot widths of 80 nm. The average insertion loss is about 2.5 dB and the mean extinction ratio is about 9.7 dB.

We designed rings with varying radii to account for fabrication variations. Extended Data Fig. 4c shows the passive spectrum of ring resonators with radii ranging from 940 nm up to 990 nm. The resonance wavelength shifts with increasing radius by $\delta\lambda_{res}/\delta R \approx 1.1$.

**Sensitivity experiments.** We used the same optical set-up as the passive characterization measurements to estimate the d.c./low-frequency electro-optic response of six devices. In a first experiment, we applied a 100 Hz triangular shaped electrical signal with a peak voltage amplitude of 10 V. We measured the modulation of the optical signal when operating the resonator around its 3 dB point. In a second experiment, we applied a d.c. bias and measured the resonators' wavelength shift as a function of the voltage. Extended Data Table 1 provides an overview of the insertion loss, extinction ratio and sensitivity of the resonance wavelength ($\Delta\lambda_{res}$ per volt) as extracted from these two experiments. The extinction ratio (6–10 dB) and insertion loss (2–3 dB) during active switching match the values obtained from passive characterization. This shows that the modulators can be driven from minimum to maximum output power before dielectric breakdown occurs. Three-dimensional simulation of device 79 revealed a $\Delta\lambda_{res}/V \approx 3.1$ nm $V^{-1}$ for an electro-optic coefficient of 100 pm $V^{-1}$. Thus, we estimate an in-device electro-optic coefficient of about 90 pm $V^{-1}$ and a $\Delta n \approx 0.03$ when biasing with ± 3.75 V based on the Pockels effect. Device 79 (last row) is shown in Fig. 3a and b of the main text.

**Speed limitations.** The electro-optic bandwidth of resonant electro-optic modulators is often determined by the photon lifetime of the resonant cavity. In the case of a ring-based electro-optic modulator with a $Q$-factor of 6,000, this equates to an electro-optic bandwidth of a few tens of gigahertz[42]. In the case of resonant plasmonic structures, the photon lifetime does not limit the electro-optic bandwidth, as these structures feature $Q$-factors that are two orders of magnitude smaller than the $Q$-factors of photonic approaches.

In general, the slowest of the following effects limits the electro-optic bandwidth of an electro-optic-modulator: (i) the $RC$ time constant; (ii) the timescale of the nonlinear effect (here the Pockels effect); and (iii) the cavity lifetime. In the case of the plasmonic MIM ring modulator presented in this work, these contributions can be approximated as follows:

- $\tau_{RC}$: The calculated capacitance of the MIM ring is approximately 1.1 fF (electrostatic 3D simulation), and its resistance is a few ohms with the nanometre-scale bridge being the main contributor[5]. This results in an RC bandwidth much greater than 1 THz.

• $\tau_{\text{Pockels}}$: The Pockels effect is based on the reorganization of $\pi$-electrons within a nanometre-long molecule and is estimated to be on the timescale of femto- or attoseconds[27]. This results in a Pockels bandwidth much greater than 1 THz.

• $\tau_{\text{cavity}}$: The SPP lifetime is given by the quality factor divided by the angular frequency ($\tau_{\text{res}} \approx Q/\omega_{\text{photon}}$). The resonant structures presented in this work feature $Q$-factors of 50, while future implementations may reach values of up to 150. Thus, the cavity lifetime of SPPs is about 100 fs or less, resulting in a cavity lifetime bandwidth limit of more than 1 THz.

Based on these approximations, we expect, at worst, a terahertz bandwidth for a plasmonic MIM resonator using the Pockels effect. To confirm that bandwidth limitations are not an issue for resonant plasmonic modulators we performed electro-optic bandwidth measurements with a plasmonic resonator of radius 1.5 μm and a designed slot width of 100 nm. These design parameters are chosen because they feature the largest $Q$-factors and therefore the longest cavity lifetimes. Extended Data Fig. 5a shows the wavelength-dependent transmittance of the plasmonic resonators and Extended Data Fig. 5b shows the normalized modulation efficiency as a function of the modulation frequency. The ratio between the unmodulated carrier and the modulated sidebands is the modulation efficiency which was measured with an optical spectrum analyser and normalized with respect to the lowest applied frequency[43].

The different colours correspond to three characteristic probing wavelengths. Red, yellow and purple are the off-resonance, 3 dB point and on-resonance probing wavelengths, respectively. For all three curves, a similar behaviour is observed, and electro-optic bandwidths beyond 100 GHz are found. This indicates that the cavity lifetime is not yet limiting the bandwidth. Otherwise, a discrepancy in bandwidth between on-resonance (purple) and off-resonance (red) operation should be observed. The kink at about 110 GHz is attributed to limitations in the electrical test set-up.

Two different measurement set-ups were required to cover the broad electrical spectrum ranging from 20 GHz up to 115 GHz in steps of 2.5 GHz. The first set-up (20 GHz to 70 GHz) used a tunable radiofrequency (RF) signal generator (100 kHz to 70 GHz) to generate a sinusoidal RF signal. The electrical output power of the source was adjusted for each frequency such that a constant power of 0 dBm was applied to the ring resonator via ground–signal–ground probes. The second set-up was used to cover the frequency range from 70 GHz to 115 GHz with a step size of 2.5 GHz. We used the sixth harmonic of a Schottky diode to generate these frequencies. The electrical input power to the Schottky diode was kept constant. We compensated the variations in the diode's output power by measuring the power with a broadband power meter. The measured power values were used in a post-processing step to subtract the influence of the varying power. The power levels of the harmonic terms other than the sixth harmonic were negligible.

Note that the signal was applied via 100 μm × 100 μm contact pads. The resonator itself (approximately 1.1 fF) does not determine the total capacitance as the large contact pads interact with the substrate resulting in a capacitance of several tens of femtofarads[44]. The modulator behaves like an open circuit element owing to the small capacitance.

**Data experiments.** This section provides details about the experimental set-up shown in Fig. 4 of the main text. A tunable, external cavity laser (1,465 nm to 1,575 nm) was used as a light source with output powers ranging from 6 dBm up to 13 dBm. The laser light was fed to an attenuator to enable a flexible adjustment of the optical power. Light was coupled to and from the chip via grating couplers, which have an efficiency ($C_{\text{GC}}$) of −7 dB each at 1550 nm.

All non-return-to-zero (NRZ) electrical data streams were random binary sequences of length $2^{18}$ generated by a 72 gigasample $s^{-1}$, six-bit digital-to-analogue converter ($f_{3\text{dB}} \approx 20$ GHz). An RF amplifier ($f_{3\text{dB}} \approx 50$–55 GHz) then amplified the electrical signal to a certain peak-to-peak driving voltage ($V_{\text{pp},50\Omega}$) measured over a 50 Ω resistor. Finally, the electrical signal was applied by ground-signal RF-probes ($f_{3\text{dB}} > 67$ GHz) to the device via 100 μm × 100 μm contact pads. Two 25-cm-long RF cables (1.85-mm connectors) connected the generator, amplifier and RF probe. The modulated light was detected coherently. We used a second laser for heterodyne detection. The 3 dB bandwidth of the coherent detector's photodiode is 70 GHz. An erbium-doped fibre amplifier amplified the optical signal after the modulator to power levels of about 8 dBm to enable best performance. The electrical oscilloscope (electrical bandwidth 63 GHz and sampling rate 160 GSa $s^{-1}$) sampled and digitized the waveform. Offline digital signal-processing was performed to account for timing errors[45], carrier frequency and phase offsets and the linear frequency response of the system by feedforward equalization with adaptive least mean square (LMS)-based filter updates. Extended Data Table 2 shows the results in terms of BER obtained from six different devices under various driving voltages ($V_{\text{peak}}$), data rates ($R$), and optical input powers at the grating coupler. Similar BERs are obtained for different devices under equal conditions. For instance, low BERs are obtained at 18 Gbit $s^{-1}$ for small driving voltages of $V_{\text{peak}} \approx 3.3$ V and low input powers. At 72 Gbit $s^{-1}$, the BER drops to $10^{-3}$ under similar conditions. We increased the driving voltages twofold and the input power fourfold and measured only a moderate reduction of the BER to $10^{-4}$. We attribute this to the limited bandwidth of the electrical components. Device 34 is shown in the Fig. 4 of the main text.

**Comparison with state-of-the-art electro-optic modulators.** In the following, we compare the plasmonic ring resonators with prior art. Electro-optic-modulators are expected to help replace electrical communication links with their optical counterparts for short-range applications. Potential candidates must be compact (footprint of a few square micrometres) to enable a dense co-integration of electronics and photonics. Furthermore, electro-optic modulators must be optimized for high speed (> 100 GHz) and low insertion loss (< 3 dB) to enable multi-gigabit operation. Extended Data Fig. 6 shows the characteristics of state-of-the-art devices (photonic, crosses; plasmonic, circles) in terms of insertion loss and electro-optic-bandwidth[5,6,18,22,43,44,46–50]. The different abbreviations represent various electro-optic materials. Ideally, modulators should occupy the bluish area at the bottom right of the figure. However, large bandwidths correlate with large insertion loss. This is because the plasmonic waveguides also serve as highly conductive electrodes, enabling a low *RC* time constant, but ohmic losses in the metals prevent low insertion losses. Conversely, the resonant switching of photonic modulators enables low losses but these suffer from limited bandwidths. Combining plasmonics and the resonant switching concept breaks the trade-off and enables high-speed and low-loss modulators.

For the convenience of the reader, we provide a detailed summary of key metrics in Extended Data Table 3 (demonstrated plasmonic modulators) and in Extended Data Table 4 (photonic electro-optic modulators). The performance of the plasmonic ring resonator (last column) serves as reference in both tables. Extended Data Table 3 compares our modulator with four non-resonant modulators based on various nonlinear effects and material systems such as $\chi^{(2)}$ in OEO materials, free-carrier dispersion (FCD) in silicon, FCD in transparent conductive oxides (TCO) and $\chi^{(2)}$ in BTO.

• The resonant approach (last column) outperforms its direct non-resonant counterpart (first column).

• Plasmonic resonators requires moderate driving voltages, and only the TCO-based modulator is driven with $V_{\text{peak}} = 1$ V as required to enable integration with electronics. However, different data rates of 72 Gbit $s^{-1}$ and 2.5 Gbit $s^{-1}$ make a comparison between our modulator and the TCO modulator challenging.

• Finally, we note that applying the resonant plasmonic approach to other material systems would enable a further boost in performance for each individual technology. For instance, one can imagine TCO-based plasmonic resonators operating with millivolt driving voltages.

Extended Data Table 4 shows six photonic modulators based on FCD in silicon[18,46], the Franz–Keldysh effect (FKE) in SiGe (ref. [48]), $\chi^{(2)}$ in BTO[47], $\chi^{(2)}$ in lithium niobate ($LiNbO_3$)[50] and Pauli blocking in graphene[51].

**Data availability.** The data that support the findings of this study are available from the corresponding author upon reasonable request.


33. Haffner, C. et al. Harnessing nonlinearities near material absorption resonances for reducing losses in plasmonic modulators. *Opt. Mater. Express* **7**, 2168–2181 (2017).
34. Jin, W. et al. Benzocyclobutene barrier layer for suppressing conductance in nonlinear optical devices during electric field poling. *Appl. Phys. Lett.* **104**, 243304 (2014).
35. Heni, W. et al. Nonlinearities of organic electro-optic materials in nanoscale slots and implications for the optimum modulator design. *Opt. Express* **25**, 2627–2653 (2017).
36. Kieninger, C. et al. In *Conf. on Lasers and Electro-Optics* STu3N.2 (Optical Society of America, 2017).
37. Maier, S. A. *Plasmonics: Fundamentals and Applications* (Springer, New York, 2007).
38. Messner, A. et al. In *Optical Fiber Communication Conf. Postdeadline Pap.* Th5C.7 (Optical Society of America, 2017).
39. Watanabe, T., Ayata, M., Koch, U., Fedoryshyn, Y. & Leuthold, J. Perpendicular grating coupler based on a blazed anti-back-reflection structure. *J. Lightwave Technol.* **35**, 4663–4669 (2017).
40. Kretz, J., Dreeskornfeld, L., Ilicali, G., Lutz, T. & Weber, W. Comparative study of calixarene and HSQ resist systems for the fabrication of sub-20nm MOSFET device demonstrators. *Microelectron. Eng.* **78/79**, 479–483 (2005).
41. Elder, D. L. et al. Effect of rigid bridge-protection units, quadrupolar interactions, and blending in organic electro-optic chromophores. *Chem. Mater.* **29**, 6457–6471 (2017).
42. Gheorma, I. L. & Osgood, R. M. Fundamental limitations of optical resonator based high-speed EO modulators. *IEEE Photon. Technol. Lett.* **14**, 795–797 (2002).
43. Hoessbacher, C. et al. Plasmonic modulator with 170 GHz bandwidth demonstrated at 100 GBd NRZ. *Opt. Express* **25**, 1762–1768 (2017).
44. Melikyan, A. et al. High-speed plasmonic phase modulators. *Nat. Photonics* **8**, 229–233 (2014).
45. Josten, A. et al. Modified Godard timing recovery for non integer oversampling receivers. *Appl. Sci.* **7**, 655 (2017).

46. Alloatti, L., Cheian, D. & Ram, R. J. High-speed modulator with interleaved junctions in zero-change CMOS photonics. *Appl. Phys. Lett.* **108**, 131101 (2016).
47. Girouard, P. et al. chi2 modulator with 40-GHz modulation utilizing $BaTiO_3$ photonic crystal waveguides. *IEEE J. Quantum Electron.* **53**, 1–10 (2017).
48. Srinivasan, A. et al. In *Optical Fiber Communication Conf.* Tu3D.7 (Optical Society of America, 2016).
49. Haffner, C. et al. Plasmonic organic hybrid modulators: scaling highest speed photonics to the microscale. *Proc. IEEE* **104**, 2362–2379 (2016).
50. Wang, C., Zhang, M., Stern, B., Lipson, M. & Loncar, M. Nanophotonic lithium niobate electro-optic modulators. Preprint at https://arxiv.org/abs/1701.06470 (2017).
51. Phare, C. T., Daniel Lee, Y.-H., Cardenas, J. & Lipson, M. Graphene electro-optic modulator with 30 GHz bandwidth. *Nat. Photon.* **9**, 511–514 (2015).

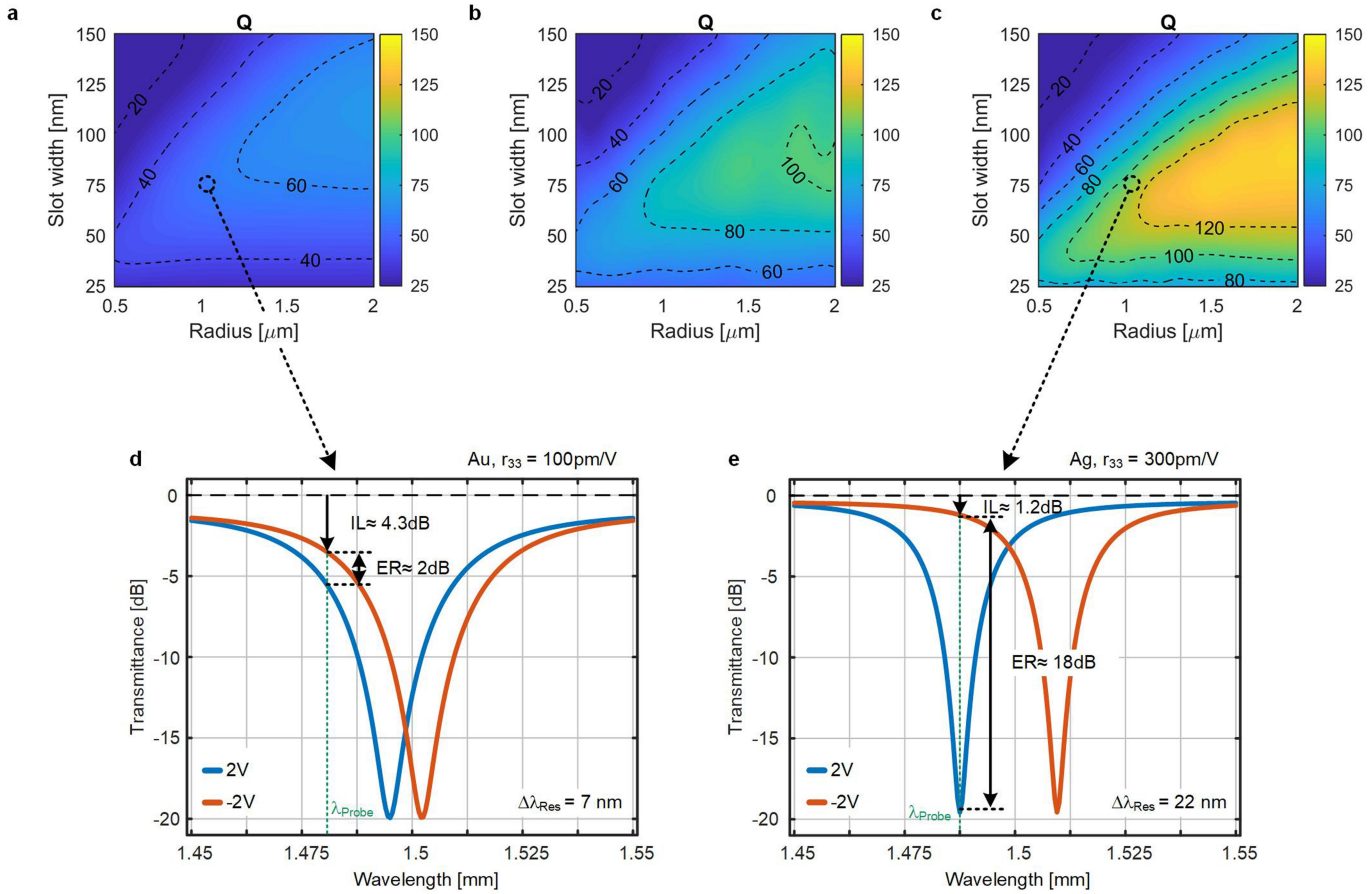


**Extended Data Fig. 1 | Resonator performance for various plasmonic materials. a**, Gold, which is interesting for research because of its chemical stability. **b**, Copper is of interest as it is a CMOS-compatible material. **c**, Silver features the best plasmonic properties and could be of interest for high-performance applications. **d**, **e**, Switching capability of (**d**) Au and (**e**) Ag ring resonator for a 2 V bias. The latter uses the newest OEO material, which has a three times larger electro-optic coefficient, $r_{33}$. The performance improvement enables a considerable reduction in terms of the driving voltage. The number at the bottom right indicates the shift in the resonance wavelength.

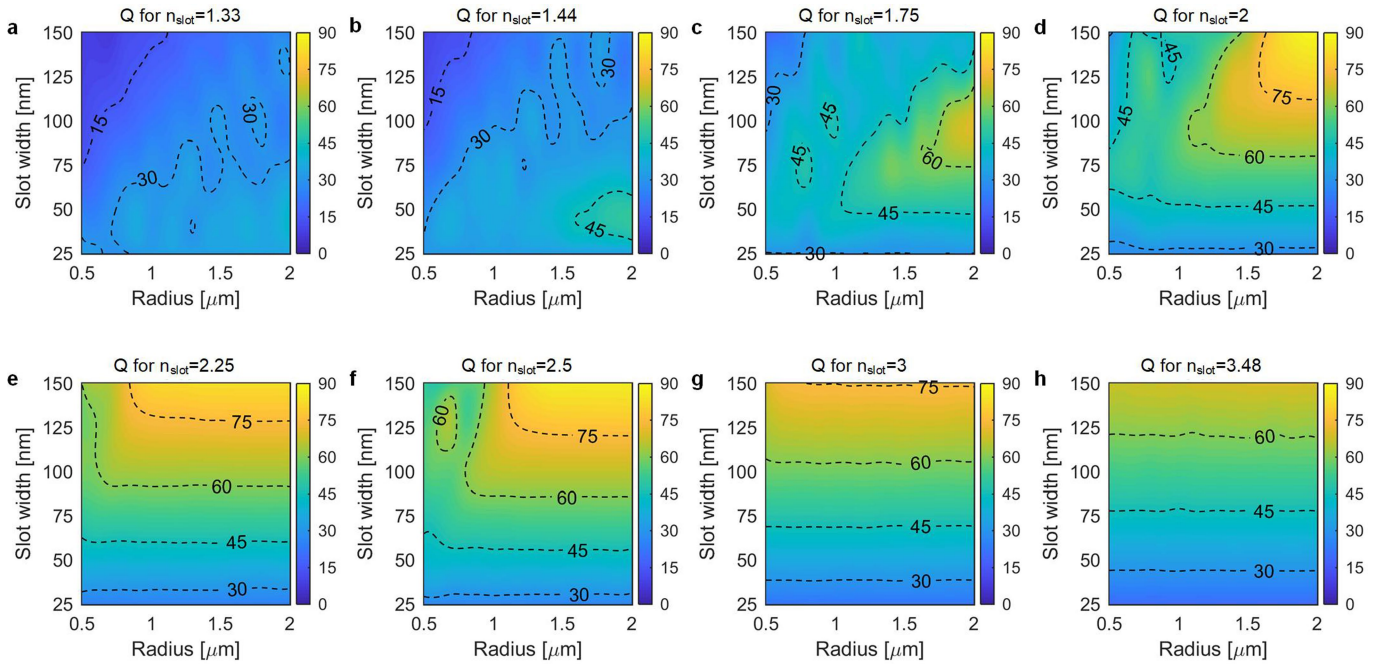


**Extended Data Fig. 2 | *Q*-factors of various materials filling the slot.** **a**–**h**, The materials differ in their refractive index, and one can observe that low-*n* materials are limited by bending loss (diagonal lines) whereas high-*n* materials are limited by propagation loss (parallel lines). These simulations were performed with 150 nm height of the outer and inner electrode to account for limitations in fabrication processes different from ours.

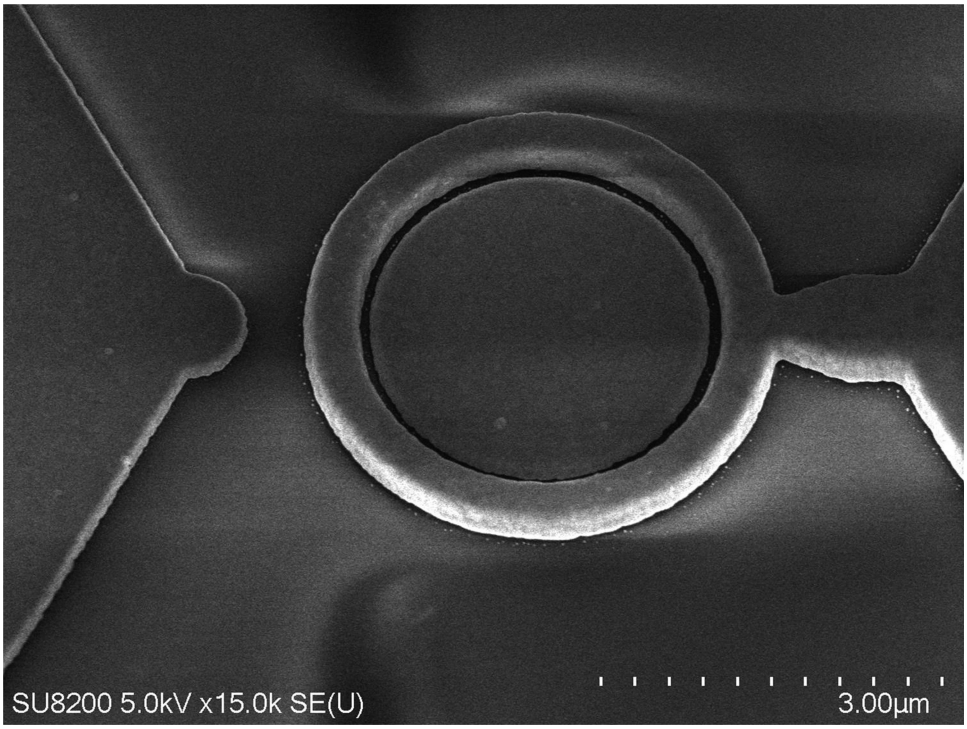


**Extended Data Fig. 3 | Tilted SEM image of a processed ring resonator.** The different height of the outer and inner electrodes reduces the bending losses.

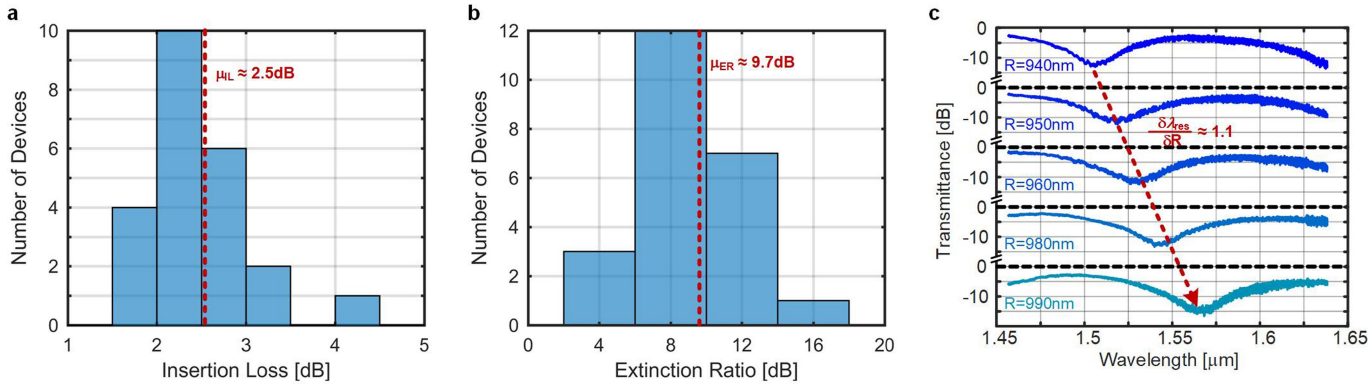


**Extended Data Fig. 4 | Reproducibility of plasmonic ring resonators.** **a**, Insertion loss and **b**, extinction ratio histograms. Data are obtained from passive measurements of 23 devices with a designed slot width of 80 nm and radii ranging from 900 nm to 1,100 nm. **c**, Dependence of the resonance wavelength on ring radius.

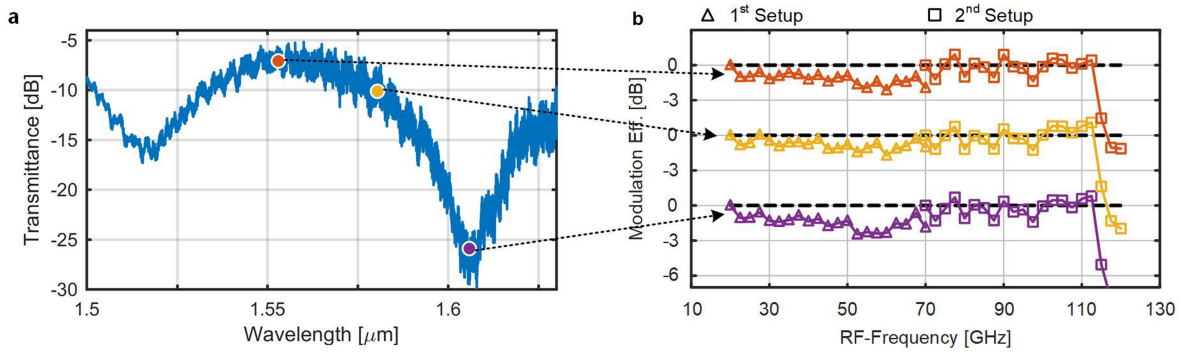


**Extended Data Fig. 5 | Transmission spectrum and the measured bandwidth at the off-resonance, 3 dB and on-resonance operating point. a**, Transmission spectrum; **b**, measured bandwidth. No bandwidth limitation can be observed up to 110 GHz. The drop at 115 GHz frequencies is due to a limited measurement set-up. Recent studies show that the modulation efficiency at lower radiofrequency is not limited[44].

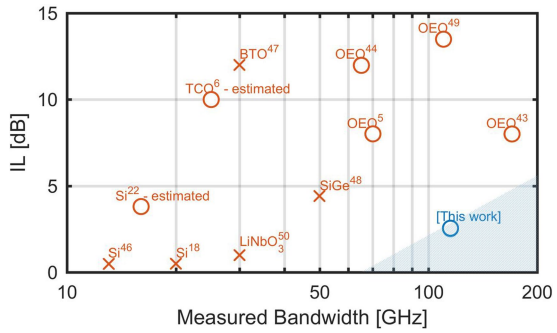


**Extended Data Fig. 6 | Technology overview in terms of insertion loss and bandwidth of electro-optic modulators.** Ideal candidates should feature low insertion loss with high electro-optic bandwidths.

**Extended Data Table 1 | Measured d.c. sensitivity**

| Radius [nm]/ Slot width [nm], (Device Id) | *IL* [dB] | *ER* [dB] | $\Delta\lambda_{res}$/Bias [nm/V] |
|---|---|---|---|
| 1200/80, (22) | ~3 | 7 | 3 |
| 1260/80, (28) | ~3 | 8 | N.A. |
| 1220/100, (36) | ~2 | 8 | 1.8 |
| 1250/100, (39) | ~2 | 6 | 2.1 |
| 1280/100, (42) | ~2.5 | 7.5 | 2.33 |
| 1080/80, (79) | ~2.75 | 10 | 2.75 |

The values of the radius and the slot width are the design parameters.

**Extended Data Table 2 | Overview of the results obtained from data experiments with various devices**

| Radius [nm]/ Slot width [nm], Device Id | $V_{peak}$ [V] | Data rate (*R*) [Gbit/s] | Bit-error-ratio (*BER*) | $P_{opitcal}$ [dBm] |
|---|---|---|---|---|
| 1230/80, (25) | ~3.3 | 18 | $\sim 9 \times 10^{-6}$ | 0 |
| 1250/80, (27) | ~3.3 | 18 | $< 1 \times 10^{-6}$ | 0 |
| 1200/100, (34) | ~3.3 | 18 | $< 1 \times 10^{-6}$ | 0 |
| " | ~3.3 | 36 | $\sim 2 \times 10^{-5}$ | 4 |
| " | ~3.3 | 72 | $\sim 1 \times 10^{-3}$ | 4 |
| 960/80, (88) | ~5 | 72 | $\sim 2 \times 10^{-3}$ | 6 |
| " | ~7.8 | 72 | $\sim 8 \times 10^{-4}$ | 6 |
| 940/80, (86) | ~7.8 | 72 | $\sim 4 \times 10^{-4}$ | 12 |
| 930/80, (85) | ~7.8 | 72 | $\sim 1 \times 10^{-3}$ | 12 |

**Extended Data Table 3 | Comparison with state-of-the-art plasmonic electro-optic modulators**

| Reference | 43 | 22 | 6 | 38 | this work |
|---|---|---|---|---|---|
| Modulation Mech. | $\chi^{(2)}$ OEO | FCD Si | FCD TCO | $\chi^{(2)}$ BTO | $\chi^{(2)}$ OEO |
| IL [dB] | ~8 | ~3.8 | ~10 | 25 | ~2.5 |
| Fiber-2-fiber loss[dB] | 34 | N.A. | N.A. | N.A. | 16 |
| ER [dB] | N.A. | 6-10 | 6 | >15 | 10 |
| $L_{Active}$ [µm] | 20 | 1 | 4 | 10 | 6 |
| Bandwidth [GHz] | >170 | 16* | >2.5 | N.A. | >110 |
| Data Rate [Gbit/s] | 100 | <<1 | 2.5 | 72 | 72 |
| Driving Voltage [$V_{peak}$] | 4 | 6 | 1 | 2.8 | 3.3 |
| Energy Consumption [fJ/Bit] | 48* | ~100 | N.A. | N.A. | 12 |

*Estimated values

**Extended Data Table 4 | Comparison with state-of-the-art photonic electro-optic modulators**

| Reference | 18 | 46 | 47 | 50 | 51 | 48 | this work |
|---|---|---|---|---|---|---|---|
| Modulation Mech. | *FCD Si* | *FCD Si* | *$\chi^{(2)}$BTO* | *$\chi^{(2)}LiNbO_3$* | *Pauli Blocking Graphene* | *FKE Si Ge* | *$\chi^{(2)}$OEO* |
| IL [dB] | *~ 0.5* | *~0.5* | *>12* | *1* | *N.A.* | *4.4* | *~ 2.5* |
| ER [dB] | *12* | *10* | *N.A.* | *~7** | *30* | *4.2* | *10* |
| $L_{active}$ [μm] | *15* | *30* | *37* | *~600** | *~250* | *40* | *6* |
| Bandwidth [GHz] | *~17* | *13* | *30** | *30* | *30* | *>50* | *>110* |
| Data Rate [Gbit/s] | *44* | *12* | *N.A.* | *40* | *22* | *50* | *72* |
| Driving Voltage [$V_{peak}$] | *0.5* | *2.46* | *16* | *2.88* | *3.75* | *1* | *3.3* |
| Energy Consumption [fJ/Bit] | *<1* | *N.A.* | *N.A.* | *240* | *800* | *13.8* | *12* |
| Q | *6000* | *15000* | *N.A.* | *8000* | *<1200* | *N.A* | *50* |
| Temp. Stability [$\Delta\lambda_{res}$ $K^{-1}$ $FWHM^{-1}$] | *100%* | *N.A.* | *N.A.* | *N.A.* | *N.A.* | *N.A* | *0.4%* |
| Sensitivity [$\Delta\lambda_{res}$ $V^{-1}$ $FWHM^{-1}$] | *100%* | *11%* | *N.A.* | *N.A.* | *N.A.* | *N.A* | *5%* |